ABSTRACT

Objective: to test the null hypothesis that chitosan application has no impact on the remineralisation of artificial incipient enamel white spot lesions (WSLs).

Methods: 66 artificial enamel WSLs were assigned to 6 experimental groups (n = 11): (1) bioactive glass slurry, (2) bioactive glass containing polyacrylic acid (BG+PAA) slurry, (3) chitosan pre-treated WSLs with BG slurry (CS-BG), (4) chitosan pre-treated WSLs with BG+PAA slurry (CS-BG+PAA), (5) remineralisation solution (RS) and (6) de-ionised water (negative control, NC). Surface and cross-sectional Raman intensity mapping (960 cm^{-1}) were performed on 5 samples / group to assess mineral content. Raman spectroscopy and attenuated total reflectance Fourier transform infrared spectroscopy (ATR-FTIR) were used to identify the type of newly formed minerals. Surface and cross-sectional Knoop microhardness were implemented to evaluate the mechanical properties after remineralisation. Surface morphologies and Ca/P ratio were observed using scanning electron microscopy (SEM) coupled with energy dispersive X-ray spectroscopy (EDX). Data were statistically analysed using one-way ANOVA with Tukey's test.

Results: BG+PAA, CS-BG, RS presented significantly higher mineral regain compared to NC on lesion surfaces, while CS-BG+PAA had higher subsurface mineral content. Newly mineralised crystals consist of type-B hydroxycarbonate apatite. CS-BG+PAA showed the greatest hardness recovery, followed by CS-BG, both significantly higher than other groups. SEM observations showed altered surface morphologies in all experimental groups except NC post-treatment. EDX suggested a higher content of carbon, oxygen and silicon in the precipitations in CS-BG+PAA group. There was no significant difference between each group in terms of Ca/P ratio.

Conclusions: The null hypothesis was rejected. Chitosan pre-treatment enhanced WSL remineralisation with either BG only or with BG-PAA complexes. A further investigation using dynamic remineralisation/demineralisation system is required with regards to clinical application.

Keywords: bioglass; polyacrylic acid; chitosan; Raman; remineralization; dental caries.

Conflicts of interest: none

1. Introduction

Dental caries is the most prevalent non-communicable oral disease [1] [2]. The white spot lesion (WSL) is the earliest clinical sign of the dental caries process, manifesting as a white chalky lesion on a susceptible dental hard tissue enamel surface that could be observed with the naked eye which intensifies when carefully dried [3]. A WSL is caused by acid attack produced by bacteria from the overlying dental plaque biofilm which covers tooth surface [4] [5]. Dissolved mineral ions, mainly Ca^{2+} and PO_4^{3-}, that leave a porous subsurface lesion, are partly retained on the newly demineralised enamel surface by the biofilm and reprecipitate to form a dense surface layer with reduced porosity (1 – 2 vol%), namely the surface zone [4].

Remineralising agents, including fluoride, nano-hydroxyapatites, functionalised tricalcium phosphates, casein phosphopeptide-amorphous calcium phosphate (CPP-ACP), have all been applied to arrest and repair WSLs either *in vitro* or *in vivo* [6] [7] [8] [9] [10]. NovaMin™ is a bioactive glass-based biomaterial that can function as a source of Ca/P ions during remineralisation to form hydroxycarbonate apatite [11]. In-vitro study has shown NovaMin™ to have potential in promoting remineralisation of incipient enamel lesions alone or in conjunction with other materials [12]. Milly et al. introduced polyacrylic acid (PAA) to enhance the bioactive glass' remineralisation potential [9]. After a 7 day in-vitro remineralisation without mechanical agitation, greater surface Knoop microhardness and higher phosphate content were recorded as well as obvious mineral depositions on lesion surface treated by BG-PAA compared to the untreated control, showing BG-PAA slurry effectively remineralised the surface of WSLs. A further study using BG-PAA as air-abrasion powder to pre-treat WSL surfaces before in-vitro remineralisation using BG-PAA slurry also found that BG-PAA successfully induced surface remineralisation [10]. Nevertheless, there is a paucity of

evidence with regards to any subsurface remineralisation effect of such topical agents. It appears any remineralisation is limited to the superficial surface where the agent is applied, which is also an issue when using other materials such as fluoride [4]. When topical agents react and remineralise readily, the already limited superficial surface porosities will be blocked, thus hindering further penetration of ions into the deeper aspect of the lesion. Therefore, this delivery of mineral ions is pivotal to obtaining complete repair of the WSL [13].

Chitosan is an *N*-deacetylated derivative product of chitin found naturally in the shell of arthropods [14]. It has attracted much attention as a functional biomaterial due to its ready availability, biocompatibility, biodegradability and non-toxicity [15] [16] [17] [18] [19]. Its high nitrogen content makes chitosan a potential vehicle to carry ions such as calcium and phosphate for biomineralisation [16] [20]. Chitosan causes a significant reduction in formation of the dental plaque biofilm through inhibition of the growth of mutans streptococci due to the positively-charged chitosan binding to negatively-charged s. mutans cell surfaces, so bridging adjacent cells thus preventing further colonisation [21] [22]. The positive charge of chitosan allows it to adhere to negatively-charged surfaces, including demineralised enamel [23] [24]. Despite being extensively used in tissue engineering, food and nutrition and drug delivery [25] [26] [27] [28], reports of including chitosan in early enamel caries treatment are sparse. Recently, chitosan has been used to remineralise enamel lesions. Chitosan-amelogenin (CS-AMEL) hydrogel was shown to induce in-vitro biomimetic remineralisation on either etched enamel or artificial enamel lesions [29] [30] [31]. Enamel-like crystals formed, and lesion depth decreased. Remineralisation didn't cease even when the pH decreased below 6.5 due to adhesion provided by the amino groups of chitosan through

electrostatic interactions. This suggests chitosan may be a suitable candidate for repairing enamel white spot lesions.

The aim of this study was to evaluate the remineralisation effect of artificial incipient white spot lesions pre-treated with chitosan, using NovaMin™ or NovaMin™/PAA as remineralising agents. Raman spectroscopy including intensity mapping, ATR-FTIR, Knoop microhardness and scanning electron microscopy were used to assess mineral content, chemical composition, mechanical properties and morphologies, respectively, as reported in other studies [9] [10]. The null hypothesis was that chitosan pre-treatment cannot enhance remineralisation of either NovaMin™ or NovaMin™/PAA.

2. Materials & Methods

2.1 Lesion formation

Ethical approval was obtained from NHS Health Research Authority (Reference 16/SW/0220). Seventy-two caries-free enamel slabs were cut from healthy human molar teeth (buccal and lingual sides) stored in deionised water using a low-speed cutting machine with water-cooled diamond saw (Labcut 1010, Agar scientific Ltd, UK), and rinsed with deionised water. Each was included in acrylic resin (Oracyl™, Bracon, UK) in a customised mould for 1 h to set, with the natural outer enamel surface facing downwards. The surfaces were ground and polished (LabForce-100, Struers, Denmark) with SiC waterproof abrasive paper in the following sequence: P500 for 10 s, P1200 for 15 s, P2000 for 30 s and P4000 for 2 min. Ultrasonication was performed for 1 min between each step and 4 min after P4000. Finished surfaces were covered by red nail varnish (Lasting Gel Nail Colour, Collection, UK) leaving a working window (approx. 1mm wide and 3mm long).

Demineralisation was carried out using a double-layer acidic gel system, containing 8 wt% methylcellulose gel and 0.1M lactic acid [9]. The gel was prepared by adding

boiling deionised water into methylcellulose powder (Sigma-Aldrich, USA) and magnetically stirred for 3 h until the gel reached room temperature. The pH of lactic acid (AnalaR, UK) was adjusted to 4.60 by 1 M NaOH. A maximum of five samples were placed on the base of one glass beaker. 100 mL gel and 100 mL acid solution were sequentially added into each beaker with filter paper in between. Beakers were sealed tightly with cling film and transferred into an incubator (MIR-262, Sanyo, Japan). The demineralisation was performed at 37°C for 21 days. Demineralisation solutions were refreshed on a weekly basis.

After lesion formation, acidic gel was removed from sample surfaces and rinsed under running deionised water. Nail varnish was removed by acetone, followed by rinsing under running deionised water. Lesions were stored in fridge at 4°C before use.

2.2 Initial characterisations of artificial lesions post chitosan pre-treatment

Preparation of chitosan solution was adapted from Arnaud et al. [32]. 25 mg chitosan was dissolved in 10 mL acetic acid (0.1 M) and stirred over night at room temperature to form an aqueous solution with a concentration of 2.5 mg/mL.

Six lesions were assigned for two groups (n = 3): (1) 1-min treatment, and (2) untreated control. 20 µL of chitosan solution was applied on carefully dried lesion surfaces for 1 minute, followed by rinsing with deionised water. Afterwards, all six lesions were hemi-sectioned to obtain two halves per sample. One half was used for surface characterisation and the other for cross-sectional. The cross-sections were polished to P4000 using above protocol and rinsing under deionised water instead of ultrasonication due to the potential collapse of lesion structure. After preparation, samples were dried with compressed air and sputter-coated with gold.

A scanning electron microscope (JCM-6000, JEOL, Japan) with a built-in energy-dispersive spectrometer (EDS) was utilised to investigate the morphologies and quantify the elemental compositions. Acquisitions were carried out using secondary electron or back-scattered electron mode with an accelerate voltage of 10 kV or 15 kV for imaging and energy-dispersive X-ray (EDX), respectively. For EDX, acquisition was performed on the entire scanned area of each sample.

2.3 Group assignment

The remaining sixty-six samples were assigned to six groups (n = 11): (1) NovaMin^{TM} (BG) slurry, (2) NovaMin^{TM} containing polyacrylic acid (BG+PAA) slurry, (3) chitosan pre-treated WSLs with NovaMin^{TM} slurry (CS-BG), (4) chitosan pre-treated WSLs with NovaMin^{TM}+PAA slurry (CS-BG+PAA), (5) remineralisation solution (RS) and (6) de-ionised water (negative control, NC).

2.4 Surface Raman intensity mapping before treatment

Five samples from each group were used for Raman intensity mapping before treatment. The acquisition was carried out by a micro-Raman spectrometer (inVia Raman Spectroscopy, Renishaw, UK) assembled with a 1200 line/mm grating, using Streamline^{TM} mode at the wavelength of 785 nm. The scanning area was determined by drawing a rectangle on a montage image which included lesion area and untouched sound enamel on both sides. Each area contained 91,000 acquisition points with a step size of 2.7 μm in x and y direction. 960 cm^{-1} was chosen as the monitored peak because it is the strongest peak of phosphate in tooth enamel and can be used to indicate the mineral content [33].

After acquisition, all data were processed using in-house software. Fitted peak height map was analysed by ImageJ (NIH, US) for mineral content quantification. The mineral content of the lesion area was calculated. The intensity ratio of lesion/sound enamel

(I_{lesion}/I_{sound}) at 960 cm^{-1} was recorded to indicate the mineral content of the artificial lesion assuming sound enamel was 100 % in mineral content for all samples.

2.5 Remineralisation regime

Chemical compositions of all remineralisation agents are listed in **Table 1**. All chemicals were purchased from Sigma-Aldrich, US except NovaMin™ (GlaxoSmithKline, UK). To prepare BG slurry (1 g/mL), 1 g powder was fully mixed with 1 mL deionised water using a whirlmixer for 1 min. To prepare BG-PAA slurry (1 g/mL, 60/40 wt/wt), 0.6 g BG, 0.4 g PAA powder and 1 mL deionised water were mixed by a whirlmixer for 1 min.

Before remineralisation, sound enamel was protected with acid-resistant tape to avoid contact with remineralising agents. Remineralisation was performed without any mechanical agitation. All samples were fitted in 6-well cell culture plate (CELLSTAR®, Greiner Bio-One, Austria). For chitosan pre-treatment, 20 μL chitosan solution was applied on the lesion surface for 1 min, then rinsed off under running deionised water. 40 μL of BG or BG+PAA slurry was applied directly onto the lesion surface immediately after preparation. To maintain the humidity during the whole regime, deionised water was added into each well until the base was covered whilst ensuring water didn't reach the sample surface level. For RS and NC group, solution was added until the sample was fully immersed. Plates were sealed and transferred to incubator at 37°C for 7 d. All remineralising agents including chitosan pre-treatment were refreshed every day.

After remineralisation, samples were rinsed with running deionised water to remove any remnants on the lesion surfaces. Protection tape was removed, and samples were stored in deionised water at 4°C before use.

2.6 Characterisations post-treatment

To study the change of surface mineral content post treatment, Raman Streamline^{TM} scanning was repeated on the same samples used in section 2.4 at the same test area. The change of I_{lesion}/I_{sound} was calculated as:

$$\text{Intensity change} = (I_{lesion} / I_{sound})_{after} - (I_{lesion} / I_{sound})_{before}$$

In addition, Raman spectra were collected on five points per sample.

Surface microhardness (SMH) was carried out on the same samples by a microhardness tester fitted with a Knoop diamond indenter (Duramin, Struer, Denmark). A load of 10 gf with 5 s dwelling were used. For each sample, 10 indentations were measured with a spacing of at least 50 μm.

These lesions were further hemi-sectioned and polished following the same procedure described in section 2.2. One half was assigned for cross-sectional Raman intensity mapping and the other half for cross-sectional microhardness. The same method in section 2.3 was used to generate cross-sectional Raman intensity maps. After acquisition and fit analysis, fitted peak height was analysed by ImageJ (NIH, US) with a customised macro to quantify the mineral content across the lesion depth. Mineral content at lesion depth of 10, 20 and 30 μm was calculated. Cross-sectional Knoop microhardness (CSMH) was conducted at the lesion depth of 20 μm. 10 gf load and 5 s dwell time were applied to make each indentation. Due to the limitation of lesion size, only 3 indentations were implemented for each sample with spacing approximating to 100 μm.

Another three lesions per group were characterised by attenuated total reflectance Fourier transform infrared spectroscopy (ATR-FTIR). Absorbance spectra in the frequency range of 550-4000 cm^{-1} were collected using an FTIR Golden Gate

spectrometer (Spectrum One, Perkin-Elmer, Beaconsfield, UK). Lesion surfaces were aligned to the diamond crystal and pressed onto its surface using consistent pressure. For each sample, 16 spectra were collected. The resultant spectra were normalised to the strongest peak in the range of 800 to 1200 cm^{-1}.

The remaining three samples in each experimental group were used for morphological observations and elemental analysis using a desktop scanning electron microscope (JCM-6000, JEOL, Japan) equipped with a built-in energy-dispersive spectrometer. Cross-sections were obtained by fracturing lesions in order to avoid artefacts caused by sectioning/polishing methodology. One half was used for surface observations and the other for cross-sectional. All specimens were sputter-coated with gold for both imaging and elemental analysis. Imaging was performed in secondary electron mode with accelerate voltage of 10 kV whilst EDX in backscattered electron mode with 15 kV acceleration voltage.

2.7 Statistical analysis

All Raman and microhardness data were statistically analysed using one-way ANOVA with Tukey's post- hoc test carried out in SPSS 23 for Windows (IBM, USA). Before ANOVA analysis, the normality and homogeneity of all data were checked by Shapiro-Wilk test and Levene test, respectively.

3. Results

3.1 SEM of lesions post chitosan pre-treatment

Fig. 1 summarises the representative SEM micrographs of the cross-section of untouched artificial white spot lesions. A typical surface layer and porous subsurface (body of the lesion) can be distinguished from **Fig. 1a**. The lesion depth ranges from 120 to 150 μm. Magnified observation reveals that the surface layer has a relatively intact structure (**Fig. 1b**). The thickness of the surface layer varies from 10 to 15 μm.

Fig. 2 shows the surface morphologies and EDX spectra of untreated lesions and lesions received chitosan pre-treatment. Untreated surface demonstrates a rough morphology with clear prism patterns along with some porosities (**Fig. 2a**). Pre-treatment by chitosan solution did introduce some alterations on the lesion surface, showing enlarged intervals between some crystals and some agglomerations (**Fig. 2b**). However, treated surfaces did not show deep, large pores, suggesting no deep erosion/etching took place. EDX suggest that chitosan pre-treatment gave rise to the content of nitrogen on the surfaces ranging from 1.60 to 6.15 at%, whereas in untreated surfaces it was less than 2 at%.

3.2 Raman intensity mapping

Surface mineral content change pre- and post-remineralisation was analysed by Raman Streamline^{TM} intensity mapping, as shown in **Fig. 3**. After 7d static remineralisation, all experimental groups showed an increased intensity ratio (**Fig. 3a**). The increase in BG+PAA, CS-BG and RS group was significantly greater when compared to NC ($p < 0.05$). However, any intensity changes in BG and CS-BG+PAA group were not significant. In the NC group, the change was found to be negative. **Fig. 3b** and **3c** presented intensity maps of CS-BG+PAA group before and post-treatment. Before remineralisation, intensity was found to be weak in the lesion area (dark colour) and strong in sound enamel on both sides (bright colour). After remineralisation, intensity increased, but not homogeneously.

Surface Raman spectra are depicted in **Fig. 4**. Characteristic phosphate peaks were observed at 961, 430 to 446, 1030 to 1045, 579 to 608 cm^{-1}, in all groups, which are assigned to $v1$ asymmetric bending vibration, $v2$ symmetric bending vibration, $v3$ asymmetric stretching vibration and $v4$ asymmetric stretching vibration of PO_4^{3-} group [34] [35] [36]. A peak at 1071 cm^{-1} was also found in all groups with various intensities.

This peak was co-contributed by *v*3 PO_4^{3-} vibration and *v*1 CO_3^{2-} vibration. It can be seen from the inset that the intensity at 1071 cm^{-1} is greater than that at 1045 cm^{-1} in BG and CS-BG groups, whereas similar in BG+PAA and CS-BG+PAA and weaker in RS and NC, indicating the formation of type-B hydroxycarbonate apatite (B-HCA) occurred in all experimental groups except RS [37]. Peak intensity ratios of 430 cm^{-1} to 446 cm^{-1} and 579 cm^{-1} to 589 cm^{-1} of experimental groups don't present significant change compared to those in NC.

The subsurface mineral content was analysed by Raman intensity mapping (**Fig. 5**). CS-BG+PAA group had the greatest mean intensity at all lesion depths (10, 20 and 30 μm) and was significantly higher than BG+PAA, RS and NC at 10 and 20 μm ($p < 0.05$). The intensity ratio of BG, BG+PAA and CS-BG groups was similar throughout measuring points and no significant difference was found between each group, while RS and NC showed the weakest. When approaching deeper towards the lesion body, all samples showed the same decreasing trend of intensity ratio. In addition, there was no significant difference between any groups at 30 μm. **Fig. 5b** illustrated a representative intensity map of the cross-section of CS-BG+PAA after remineralisation. The entire lesion presented a ditch-like shape with a clear boundary.

3.3 ATR-FTIR

Representative ATR-FTIR spectra of the lesion surface post remineralisation are shown in **Fig. 6**. The strongest band was found at ~ 980 to 1000 cm^{-1}, which could be attributed to *v*3 PO_4^{3-} vibration. A shoulder band was also observed at ~ 950 cm^{-1}, which can be assigned to *v*1 PO_4^{3-} vibration [38]. From the spectra, it can be seen that redshift of *v*3 PO_4^{3-} vibration band took place in all experimental groups except RS when compared to NC, from 1000 to 990 cm^{-1}. A band at ~ 867 cm^{-1} was found in all groups including NC, which is attributed to *v*2 CO_3^{2-} vibration (type-B) [38]. *v*3 CO_3^{2-} vibration

contributes to two overlapping bands at 1400 to 1500 cm^{-1} [38]. No band at 880 cm^{-1} was seen in all groups, indicating that type-A HCA didn't form on the lesion surface. These two CO_3^{2-} bands show a relatively low intensity in NC, but increased in BG or CS-BG. Whilst in BG+PAA and CS-BG+PAA, the increase was dominantly seen for *v*2 CO_3^{2-} vibration band, which is also found in RS. These suggest that the newly form minerals included type-B HCA.

3.4 Microhardness

Mechanical properties of the lesion on both surface and cross-section (20 μm) were recorded as mean ± standard deviation, using Knoop microhardness (**Fig. 7**). CS-BG+PAA exhibited the highest surface microhardness (222.2 ± 37.7 KHN) and was statistically higher when compared to other groups ($p < 0.05$). The surface microhardness of CS-BG was 142.4 ± 28.1. BG and BG+PAA group showed similar microhardness values after remineralisation (103.6 ± 6.5 and 95.5 ± 9.8, respectively), while no significant difference was found when compared to RS and NC (61.3 ± 17.3 and 52 ± 21.2, respectively).

With respect to cross-sectional Knoop microhardness (**Fig. 7**), chitosan treated groups both exhibited higher hardness values than other groups. The greatest hardness was found to lie within CS-BG+PAA group and was significantly higher than remaining groups ($p < 0.05$). CS-BG also showed a significantly higher hardness value than BG ($p < 0.05$).

3.5 Ultrastructural observations

Representative SEM micrographs of all groups post-treatment are summarised in **Fig. 8** and **Fig. 9**. Typical enamel prismatic "*key-hole*" structures in NC could be recognised along with small pores as shown in **Fig. 8f**. Depositions on the surface (black arrow)

could also be seen. RS shows similar morphology except deposition. In BG treated group (**Fig. 8a**), the surface was covered by densely packed precipitations, although pores can still be found (black arrow). BG+PAA (**Fig. 8b**) showed more intact prism morphology compared to NC. While for chitosan pre-treated groups, different morphologies were found. Both CS-BG (**Fig. 8c**) and CS-BG+PAA (**Fig. 8d**) illustrated unevenly distributed patchy-like precipitations without obvious pores (red arrows), despite there are still pores around.

Fig. 9 showed subsurface structures of fractured lesions post-treatment. As shown in **Fig. 9e** and **9f**, oriented prism (rod, R) and inter-prism (inter-rod, IR) could be seen throughout the subsurface in RS and NC. In BG group (**Fig. 9a**), superficial surface was covered by a thin newly formed layer, whereas in BG+PAA, a similar layer was also present as seen in **Fig. 9b** (red arrows). CS-BG showed a disrupted subsurface structure with less oriented precipitations (**Fig. 9c**). For CS-BG+PAA (**Fig. 9d**), a denser structure was observed, and the typical prismatic structure was absent when compared to NC.

3.6 Elemental analysis

EDX analysis (**Fig. 10**) revealed that the remineralised surface of all groups was not composed of pure hydroxyapatite in which the calcium phosphate (Ca/P) ratio is 1.67. For each group the ratio was 1.54 ± 0.03 (BG), 1.58 ± 0.02 (BG+PAA), 1.57 ± 0.04 (CS-BG), 1.56 ± 0.09 (CS-BG+PAA), 1.56 ± 0.02 (RS) and 1.54 ± 0.02 (NC). Ca/P ratio between each group was not statistically different. Elements recognised included calcium, phosphate, carbon, oxygen and gold for all groups, except for CS-BG+PAA in which a weak peak of silicon was also present. The atomic amount of gold was approximately 1 %.

Particles on the surface of CS-BG+PAA samples (**Fig. 10c**) were also investigated by EDAX. Ca/P ratio was 1.63, which was higher than that of areas not covered by these particles, but the standard deviation was also greater (0.18). Silicon, carbon and oxygen generated stronger peaks as illustrated in **Fig. 10d**.

4. Discussion

Clinical therapies introducing fluoride and other agents such as bioactive glass to remineralise incipient enamel carious lesions have been reported [9] [10] [39]. However, a limitation of these therapies is that remineralisation takes place predominantly on the lesion surface. This surface precipitation is likely to fill superficial pores and block pathways to the lesion body, giving rise to a restriction in complete lesion consolidation [13] [40] [41]. Cochrane et al. proposed a definition of remineralisation that "includes any crystal repair to bring about net mineral gain to an enamel subsurface lesion, but does not extend to precipitation of solid phases onto enamel surfaces" [42]. Therefore, mineral deposition within the subsurface plays a vital role in achieving successful remineralisation. In this study, chitosan was chosen to pre-treat artificial white spot lesions to aid subsurface remineralisation of bioglass and bioglass/polyacrylic acid complexes. Arnaud et al. reported that chitosan itself could penetrate into sound enamel and its permeability has a positive correlation with its concentration [32]. In the present study, a concentration of 2.5 mg/mL as proposed by Arnaud et al. was used [32]. The dissolution of chitosan powder in acetic acid involves the breakage of hydrogen bonds and protonation of NH_2 groups. The dissolved chitosan may be small enough to pass through the pores observed in **Fig. 2**. Chitosan solution after dissolution in 0.1M acetic acid has a pH of 3.30, which opens gaps between crystals in the surface layer, which could also aid the penetration of chitosan. Chitosan treatment for 1 minute did not

induce deep erosion/etching as such pattern was not observed in **Fig. 2**. The positive identification of nitrogen in treated lesions confirmed the presence of chitosan, which may be assisted by ionic interactions between positively charged nitrogenous species and demineralised enamel prisms.

Surface Raman intensity mapping shows that I_{lesion}/I_{sound} ratio of all experimental groups increased after 7d static remineralisation (**Fig. 3a**) indicating that surfaces were remineralised by the materials employed. A few samples treated by deionised water showed a negative change, this is due to the fact that carbonic acid forms in deionised water when in contact with carbon dioxide from the atmosphere. The actual pH of deionised water used in this study was 5.6 hence is able to cause demineralisation of the lesion. The increases in BG+PAA, CS-BG and RS group were statistically greater compared to NC group ($p < 0.05$).

In comparison with BG group, chitosan pre-treatment led to an increasing tendency of surface remineralisation, despite this is not statistically significant ($p > 0.05$). For CS-BG+PAA, a smaller increase is observed without chitosan pre-treatment, which was unexpected. This is probably due to the short remineralisation period. Raman spectroscopy is also a surface characterisation technique with limited depth profiling ability. Tfaili et al. found that Raman signal intensity was attenuated to 80 % at 6 μm beneath the surface of a pig ear skin when excited by a laser beam with 785 nm wavelength and exposure time of over 2 h [43]. In the present study, the actual exposure time on each data point was less than 0.1 s, using the same laser wavelength of 785 nm. Since detection is restricted to a depth of a few microns, Raman intensity mapping is very sensitive to surface morphology. It can be seen from **Fig. 10c** that the lesion surface in CS-BG+PAA was partly masked by large particles, which can impact the

intensity mapping. We therefore suspect that the lower increase in CS-BG+PAA may not represent the true value.

Raman spectra of remineralised lesion subsurfaces reveal the type of newly formed minerals. The reaction of bioglass involves the formation of carbonate-substituted apatite [44] [45]. Carbonate substitutes in two ways: by replacing phosphate groups which yield type-B HCA and replace hydroxyl groups which yield type-A HCA [46] [47]. Type-A and -B HCA generate Raman peaks at ~ 1070 and ~ 1103 cm^{-1}, respectively [46]. However, phosphate groups also contribute to the peak at 1071 cm^{-1} making this region complicated, explaining its appearance in NC. Despite the complexity, the disappearance of peak 1103 cm^{-1} and the increased intensity ratio of 1071 to 1045 cm^{-1} peaks in experimental groups (except RS) indicate that the newly formed minerals included type-B HCA rather than its type-A phase. Peak intensity ratios of 430 to 446 cm^{-1} and 579 to 589 cm^{-1} don't present significant change compared to those in NC, suggesting the minerals still have caries characteristics [36].

The mineral type is further proved by ATR-FTIR spectral investigations shown in **Fig. 4**, in which $\nu 2$ CO_3^{2-} vibration generated one strong peak positioned ~ 867 cm^{-1}, confirming the formation of type-B HCA. Additionally, we note that the intensity ratio of $\nu 2$ CO_3^{2-} to $\nu 3$ PO_4^{3-} in CS-BG+PAA is greater in than that in BG+PAA, which might suggest a thicker HCA layer [48].

It is also noticed that the strongest peak generated by $\nu 3$ PO_4^{3-} vibration in NC was at 1000 cm^{-1}, which is a red shift compared to that in sound enamel [49]. This implies that crystals formed by dissolved Ca and P ions have structural defects and less stable phosphate groups. After remineralisation, this band shifted to lower wavenumber in

experimental groups except RS. This is because of the substitution of carbonate which further deforms the crystal structure.

Further Raman investigations on the lesion subsurface after remineralisation reveal that application of BG and BG+PAA post pre-treatment led to an increasing tendency with respect to intensity ratio on all depth points examined (**Fig. 5**). In groups with pre-treatment, I_{lesion}/I_{sound} ratio is higher than other groups at 10 and 20 μm subsurface. At 30 μm, there is no statistical difference between each group, implying that enhancement effect of chitosan pre-treatment has weakened at this depth. The relatively low concentration of chitosan solution could partly explain the weakened subsurface remineralisation at 30 μm. However, the increase in concentration is accompanied with higher viscosity, which may inversely reduce chitosan's permeability. Wang *et al*. suggested that when CS comes into contact with PAA, carboxylic groups in PAA would be dissociated to COO^- groups and combine with amino groups from CS by electrostatic attraction [50]. During the preparation of BG/PAA slurry, calcium cations are released rapidly from BG particles and then chelated by PAA during the preparation of the BG+PAA slurry [9] [51]. Therefore, CS in the lesion subsurface enhanced the delivery of calcium cations. Additionally, chitosan captured phosphate ions from BG+PAA slurry through electrostatic force due to the existence NH^{3+} groups. This can explain why chitosan pre-treatment only caused significant greater remineralisation when BG and PAA were present together. Without chitosan pre-treatment, BG or BG+PAA slurry still induced some subsurface remineralisation down to 20 μm. As for RS, similar subsurface mineral content like NC group was found. This could be caused by An unsuitable pH environment.

The surface and subsurface remineralisation enhanced by chitosan pre-treatment is also evidenced by Knoop microhardness. Surface hardness results shows that the greatest

hardness recovery lay within CS-BG+PAA group followed by CS-BG. This suggests that chitosan pre-treatment enhanced successfully the surface remineralisation effect of both BG and BG+PAA slurry. The large standard deviations imply that remineralisation on superficial surface is not homogenous. Due to the geometry of the Knoop indenter used in this study, the indentation depth caused by surface microhardness test was approx 1 μm. Accurate microhardness measurements can only be obtained on homogenous, flat surfaces [52] [53]. Therefore, the precipitations on the surface as shown in SEM images (**Fig. 8**) may influence the indentation.

As revealed by SEM observations (**Fig. 1b**), the surface layer produced by the acidic gel demineralisation system was ~15 μm deep, whilst the lesion subsurface beyond 20 μm shows obvious porosities. Hence, cross-sectional microhardness was carried out at 20 μm lesion depth to investigate the penetration of remineralisation. Subsurface microhardness reveals the same tendency of hardness values of all groups as that in surface hardness. This is in agreement with previous postulation that chitosan aided the subsurface remineralisation in Raman intensity mapping. Compared to surface hardness, a dramatic decrease was recorded in all groups. This is because the subsurface had a lower mineral content than the surface layer, while mineral content is directly associated with enamel's mechanical properties [54]. The orientation of prisms also accounts for the variations of enamel's mechanical properties at different anatomical positions [55]. There is evidence that hardness is higher in an occlusal direction (parallel to prism orientation) than axially (perpendicular to prisms) [55] [56] [57]. In additional, the nature of microhardness that pushes the tip into material will cause deformation and stress. If two indentations are neighbouring, the internal stress may also affect hardness measurement. For subsurface Knoop microhardness in the present study, indenter yielded indentation up to ~ 120 μm in length. Limited by the lesions'

cross-sectional dimension (approx. 1000 μm in length and 120 μm in height, as measured in **Fig. 1**), only three indentations with spacing of approximately 100 μm to minimise stress effects were possible in this study.

Variations on surface morphologies post remineralisation were observed by SEM. Pores could be seen clearly in NC, suggesting that although the surface zone is relatively intact compared to other zones in the WSL, it still provides pathways for the infiltration of remineralising agents. The particles could be caused by the deposition of Ca and P ions dissolved by deionised water. Nevertheless, no obvious changes can be seen compared to untreated lesions shown in **Fig. 2a**. Surfaces in CS-BG and CS-BG+PAA appear patchy with obvious prism outlines. However, pores could also be seen in CS-BG+PAA, suggesting the remineralisation might not proceed homogeneously. EDX elemental analysis confirmed that the surface constituted calcium, phosphorus, carbon and oxygen and similar Ca/P ratio as in the area not covered by particles. No nitrogen was detected, which might because its content post remineralisation exceeded the detection limit of the machine. Interestingly, the surface in CS-BG+PAA group also showed notable large particles on the surface with various dimensions and shapes (**Fig. 10d**). EDX analysis illustrated that these particles contain higher amounts of silicon, carbon and oxygen, showing some similarities to bioactive glass particles. It should be mentioned that the present study didn't introduce any mechanical agitation. Hence, these particles might be the remnants of bioactive glass particles. Particles remaining even after thorough rinsing under running deionised water suggests that a strong bond is formed between particles and the remineralised surface. According to the reaction stages of bioactive glass [58], it is possible that bioactive glass particles and BG+PAA complexes formed a bonding [50], which further bonded onto the lesion surface through electrostatic attraction [23] [24]. Subsurface

observations (**Fig. 9**) revealed that CS-BG and CS-BG+PAA had a denser morphology with the absence of typical prismatic structure compared to others, implying that subsurface remineralisation have taken place and filled the pores. This explains the increasing tendency of subsurface hardness of CS-BG and CS-BG+PAA.

5. Conclusions

The null hypothesis was rejected. Chitosan improved the remineralisation efficacy using either a bioactive glass slurry alone or bioactive glass/polyacrylic acid complexes as both surface and subsurface showed an increasing tendency in mineral content assessed by Raman intensity mapping. Newly formed mineral consists of type-B HCA rather than type-A HCA. Significantly greater Knoop microhardness was found in CS-BG and CS-BG+PAA on the surface and subsurface. Irregular shaped depositions were found on the surface whereas on the subsurface prism structure these were replaced by newly formed precipitations in CS-BG+PAA. Relatively denser subsurface was seen on the subsurface of CS-BG and CS-BG+PAA than pre-treatment-free groups. With regards to clinical application, a further study involving a dynamic re-/demineralisation model is required.

6. References

[1] Katie C, Buschang PH and Campbell PM. Prevalence of white spot lesion formation during orthodontic treatment. Angle Orthod, 2013; 83: 641-647.

[2] Sundararaj D, Venkatachalapathy S, Tandon A and Pereira A. Critical evaluation of incidence and prevalence of white spot lesions during fixed orthodontic appliance treatment: A meta-analysis. J Int Soc Prev Community Dent, 2015; 5: 433-439.

[3] Kidd EAM. Essential of dental caries: the disease and its management. 3rd ed. Oxford: Oxford University Press; 2005.

[4] Robinson C, Shore RC, Brookes RC, Strafford S, Wood SR and Kirkham J. The chemistry of enamel caries. Crit Rev Oral Biol Med, 2000; 11: 481-495.

[5] Selwitz RH, Ismail A and Pitts NB. Dental caries. Lancet, 2007: 369: 51-59.

[6] Karlinsey RL, Mackey AC, Walker ER, Amaechi BT, Karthikeyan R, Najibfard K and Pfarrer AM. Remineralization potential of 5,000 ppm fluoride dentifrices evaluated in a pH cycling model. J Dent Oral Hyg, 2010; 2: 1-6.

[7] Huang S, Gao S, Cheng L and Yu H. Remineralization potential of nano-hydroxyapatite on initial enamel lesions: An in vitro study. Caries Res, 2011; 45: 460-468.

[8] Krithikadatta J, Fredrick C, Abarajithan M and Kandaswamy D. Remineralisation of occlusal white spot lesion with a combination of 10% CPP-ACP and 0.2% sodium fluoride evaluated using Diagnodent: a pilot study. Oral Health Prev. Dent, 2013; 11: 191-196.

[9] Milly H, Festy F, Watson TF, Thompson I and Banerjee A. Enamel white spot lesions can remineralise using bio-active glass and polyacrylic acid-modified bio-active glass powders. J Dent, 2014; 42: 158-166.

[10] Milly H, Festy F, Andiappan M, Watson TF, Thompson I and Banerjee A. Surface pre-conditioning with bioactive glass air-abrasion can enhance enamel white spot lesion remineralization. Dent Mater, 2015; 31: 522-533.

[11] Wefel JS. NovaMin®: Likely clinical success. Adv Dent Res, 2009; 21: 40-43.

[12] Burwell AK, Litkowski LJ and Greenspan DC. Calcium Sodium Phosphosilicate (NovaMin®): Remineralisation potential. Adv Dent Res, 2009; 21: 35-39.

[13] Amaechi BT. Remineralization therapies for initial caries lesions. Curr Oral Health Rep, 2015; 2: 95-101.

[14] Chae SY, Jang M and Nah J. Influence of molecular weight on oral absorption of water soluble chitosans. J Control Release, 2005; 102: 383-394.

[15] Rinaudo M. Chitin and chitosan: Properties and applications. Prog Polym Sci, 2006; 31: 603-632.

[16] Lin Y, Zheng R, He H, Du H and Lin Y. Application of biomimetic mineralization: A prophylatic therapy for crack teeth? Med Hypotheses, 2009; 73: 493-494.

[17] Dash M, Chiellini F, Ottenbrite RM, Chiellini E. Chitosan – a versatile semi-synthetic polymer in biomedical applications. Prog Polym Sci, 2011; 36: 981-1014.

[18] Lee H, Tsai S, Kuo C, Bassani AW, Pepe-Mooney B, Miksa D, Masters J, Sullivan J and Composto RJ. Chitosan adsorption on hydroxyapatite and its role in preventing acid erosion. J Colloid Interface Sci, 2012; 385: 235-243.

[19] Tian K, Peng M, Fei W, Liao C and Ren X. Induced synthesis of hydroxyapatite by chitosan for enamel remineralization. Adv Mat Res, 2012; 530: 40-45.

[20] Ravi Kumar MNVR. A review of chitin and chitosan applications. React Funct Polym, 2000; 46: 1-27.

[21] Muzzarelli R, Tarsi R, Filippini O, Giovanetti E, Biagini G and Varaldo PE. Antimicrobial properties of N-carboxybutyl chitosan. Antimicrob Agents Chemother, 1990; 34: 2019-2023.

[22] Sano H, Shibasaki K, Matsukubo T and Takaesu Y. Effect of chitosan rinsing on reduction of dental plaque formation. Bull Tokyo Dent Coll, 2003; 44: 9-16.

[23] Claesson PM and Ninham BW. pH-dependent interactions between adsorbed chitosan layers. Langmuir, 1992; 8: 1406-1412.

[24] Young A, Smistad G, Karlsen J, Rolla G and Rykke M. Zeta potentials of human enamel and hydroxyapatite as measured by the Coulter DELSA 440. Adv Dent Res, 1997; 11: 560-565.

[25] Koide SS. Chitin-chitosan: Properties, benefits and risks. Nutr Res, 1998; 18: 1091-1101.

[26] Mao J, Zhao L, Yao D, Shang Q, Yang G and Cao Y. Study of novel chitosan-gelatin artificial skin in vitro. J Biomed Mater Res Part A, 2003; 64A: 301-308.

[27] Devlieghere F, Vermeulen A and Debevere J. Chitosan: antimicrobial activity, interactions with food components and applicability as a coating on fruit and vegetables. Food Microbiol, 2004; 21: 703-714.

[28] Kim IY, Seo SJ, Moon HS, Yoo MK, Park IY, Kim BC and Cho CS. Chitosan and its derivatives for tissue engineering applications. Biotechnol Adv, 2008; 26: 1-21.

[29] Ruan Q, Zhang Y, Yang X, Nutt S and Moradian-Oldak J. An amelogenin-chitosan matrix promotes assembly of an enamel-like layer with a dense interface. Acta Biomater, 2013; 9: 7289-7297.

[30] Ruan Q and Moradian-Oldak J. Development of amelogenin-chitosan hydrogel for in vitro enamel regrowth with a dense interface. J Vis Exp, 2014; 89: 51606.

[31] Ruan Q, Liberman D, Bapat R, Chandrababu KB, Phark JH and Moradian-Oldak J. Efficacy of amelogenin-chitosan hydrogel in biomimetic repair of human enamel in pH-cycling systems. J Biomed Eng Inform, 2016; 2: 119-128.

[32] Arnaud TM, de Barros Neto B and Diniz FB. Chitosan on dental enamel de-remineralization: an in vitro evaluation. J Dent, 2010; 38: 848-852.

[33] Rehman I, Hench LL, Bonefield W and Smith R. Analysis of surface layers on bioactive glasses. Biomaterials, 1994; 15: 865-870.

[34] Tsuda H and Arends J. Orientational micro-Raman spectroscopy on hydroxyapatite single crystals and human enamel crystallites. J Dent Res, 1994; 73: 1703-1710.

[35] Kirchner MT, Edwards HGM, Lucy D and Pollard AM. Ancient and modern specimens of human teeth: a Fourier transform Raman spectroscopic study. J Raman Spectrosc, 1997; 28: 171-178.

[36] Ko AC, Choo-Smith LP, Hewko M, Leonardi L, Sowa MG, Dong CC, Williams P and Cleghorn B. Ex vivo detection and characterization of early dental caries by optical coherence tomography and Raman spectroscopy. J Biomed Opt, 2005; 10: 031118.

[37] Xu C, Yao X, Walker MP and Wang Y. Chemical/molecular structure of the dentin-enamel junction is dependent on the intratooth location. Calcif Tissue Int, 2009; 84: 221-228.

[38] Fleet ME and Liu X. Coupled substitution of type A and B carbonate in sodium-bearing apatite. Biomaterials, 2007; 28: 916-926.

[39] Zero DT. Dentifrices, mouthwashes, and remineralization/caries arrestment strategies. BMC Oral Health, 2006; 6: S9.

[40] Cochrane NJ, Zero DT and Reynolds EC. Remineralization models. Adv Dent Res, 2012; 24: 129-132.

[41] Lynch RJM and Smith SR. Remineralization agents – new and effective or just marketing hype? Adv Dent Res, 2012; 24: 62-67.

[42] Cochrane NJ, Cai F, Huq NL, Burrow MF and Reynolds EC. New approaches to enhanced remineralization of tooth enamel. J Dent Res, 2010; 89: 1187-1197.

[43] Tfaili S, Josse G, Gobinet C, Angiboust J, Manfait M and Piot O. Shedding light on the laser wavelength effect in Raman analysis of skin spidermises. Analyst, 2012; 137: 4241-4246.

[44] Hench LL. Bioceramics: From concept to clinic. J Am Ceram Soc, 1991; 74: 1487-1510.

[45] Hench LL. Bioceramics. J Am Ceram Soc, 1998; 81: 1705-1728.

[46] Penel G, Leroy G, Rey C and Bres E. MicroRaman spectral study of the PO_4 and CO_3 vibrational modes in synthetic and biological apatites. Calcif Tissue Int, 1998; 63: 475-481.

[47] Freeman JJ, Wopenka B, Silva MJ and Pasteris JD. Raman spectroscopic detection of changes in bioapatite in mouse femora as a function of age and in vitro fluoride treatment. Calcif Tissue Int, 2001; 68: 156-162.

[48] Notingher I, Jones JR, Verrier S, Bisson I, Embanga P, Edwards P, Polak JM and Hench LL. Application of FTIR and Raman spectroscopy to characterisation of bioactive materials and living cells. J Spectrosc, 2003; 17: 275-288.

[49] Reyes-Gasga J, Martínez-Piñeiro EL, Rodríguez-Álvarez G, Tiznado-Orozco GE, García-García R and Brès EF. XRD and FTIR crystallinity indices in sound human tooth enamel and synthetic hydroxyapatite. Mater Sci Eng C Mater Biol Appl, 2013; 33: 4568-4574.

[50] Wang H, Li W, Lu Y and Wang Z. Studies on chitosan and poly(acrylic acid) interpolymer complex. I. preparation, structure, pH-sensitivity, and salt sensitivity of complex-forming poly(acrylic acid): chitosan semi-interpenetrating polymer network. J Appl Polym Sci, 1997; 65: 1445-1450.

[51] Rossi S, Sandri G, Ferrari F, Bonferoni MC and Caramella C. Buccal delivery of acyclovir from films based on chitosan and polyacrylic acid. Pharm Dev Technol, 2003; 8: 199-208.

[52] Arends J, Schuthof J and Jongebloed WG. Microhardness indentations on artificial white spot lesions. Caries Res, 1979; 13: 290-297.

[53] Arends J, Schuthof J and Jongebloed WG. Lesion depth and microhardness indentations on artificial white spot lesions. Caries Res, 1980; 14: 190-195.

[54] Kodaka T, Debari K, Yamada M and Kuroiwa M. Correlation between microhardness and mineral content in sound human enamel. Caries Res, 1992; 26: 139-141.

[55] Meredith N, Sherriff M, Setchell DJ and Swanson SA. Measurement of the microhardness and Young's modulus of human enamel and dentine using an indentation technique. Arch Oral Biol, 1996; 41: 539-545.

[56] Craig RG and Peyton FA. The micro-hardness of enamel and dentin. J Dent Res, 1958; 37: 661-668.

[57] Xu HH, Smith DT, Jahanmir S, Romberg E, Kelly JR, Thompson VP and Rekow ED. Indentation damage and mechanical properties of human enamel and dentin. J Dent Res, 1998; 77: 472-480.

[58] Hench LL. Bioceramics. J Am Ceram Soc, 1998; 81: 1705-1728.

[59] Ten Cate JM, Exterkate RA and Buijs MJ. The relative efficacy of fluoride toothpastes assessed with pH cycling. Caries Res, 2006; 40: 136-141.

TABLE 1. Composition and concentration of applied materials

Material	Compositions
BG slurry (1 g/L)	NovaMin™ 4516 bioactive glass [a] (1 g), deionised water (1 mL)
BG+PAA complexes slurry (1 g/L)	NovaMin™ 4516 bioactive glass [a] (0.6 g), polyacrylic acid powder (0.4 g), deionised water (1 mL)
Chitosan solution (2.5 mg/mL)	Chitosan powder (25 mg), 0.1 M acetic acid solution (10 mL)
Remineralisation solution [59]	HEPES (20 mM), KCl (130 mM), $CaCl_2$ (1.5 mM), KH_2PO_4 (0.9 mM), pH adjusted to 7.0 by 1 M NaOH

[a] GlaxoSmithKline Healthcare (Weybridge, UK)

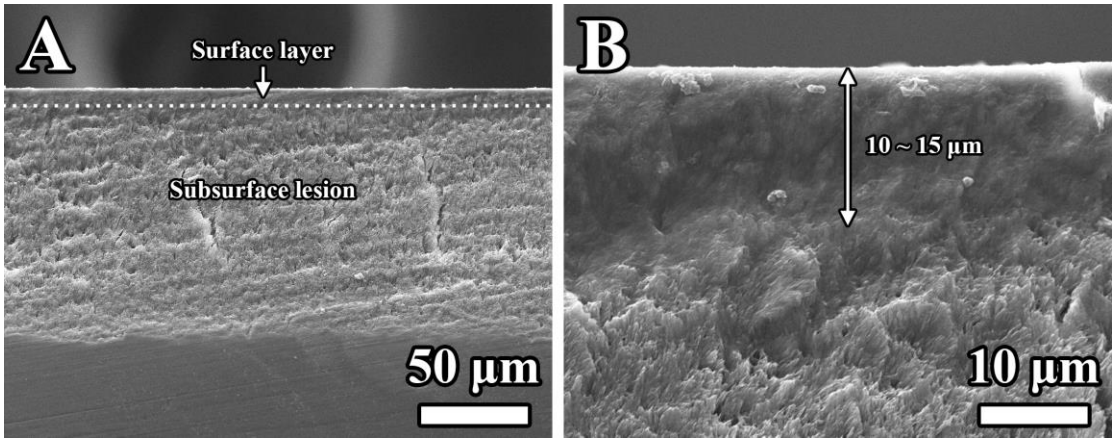

Fig. 1 Representative SEM micrographs of the artificial white spot lesion formed by the acidic gel demineralisation system at x400 (a) and x2000 (b) magnification. Typical surface layer of the WSL was found to exist above the porous subsurface (body of the lesion). The surface layer was measured to be as thick as 10 to 15 µm (b). Obvious voids (porosities) can be clearly seen beneath the surface layer, suggesting that the as-produced artificial lesion can act as an analogue of natural subsurface lesion.

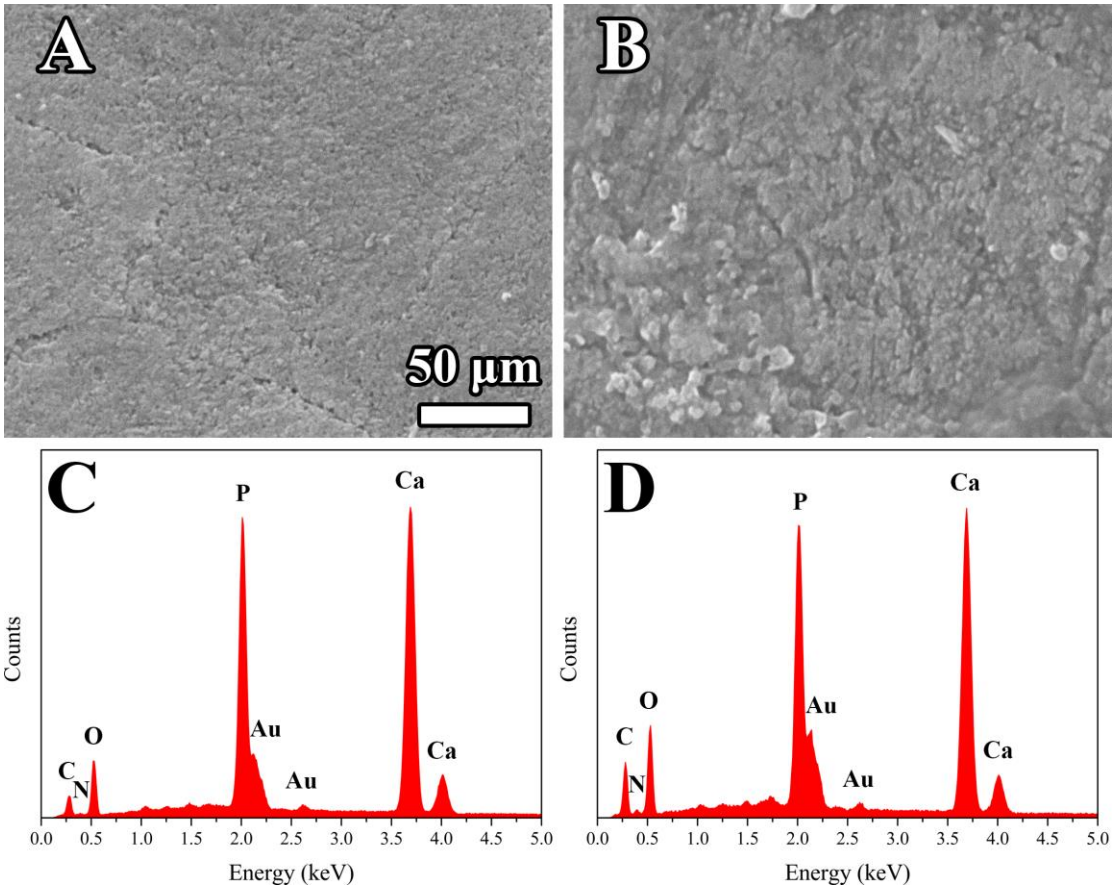

Fig. 2 Representative SEM micrographs (x10000) of untreated (a) and chitosan pre-treated lesion surfaces (b) and corresponding EDX spectra (c, d). Untreated lesion surface shows characteristic rough, porous morphology along with recognisable outline of enamel "*key-hole*" structure (a). Chitosan pre-treatment introduced some morphological alterations upon the lesion surface by enlarging the gaps between some enamel crystals as well as some agglomerations seen on the bottom left (b). No obvious deep pores can be recognised indicating that aggressive erosion/etching didn't take place. EDX spectra reveal that nitrogen exists in both lesion surfaces. The nitrogen content increased to 1.60 to 6.15 at% after chitosan treatment, whereas for untreated surface it was less than 2 at%.

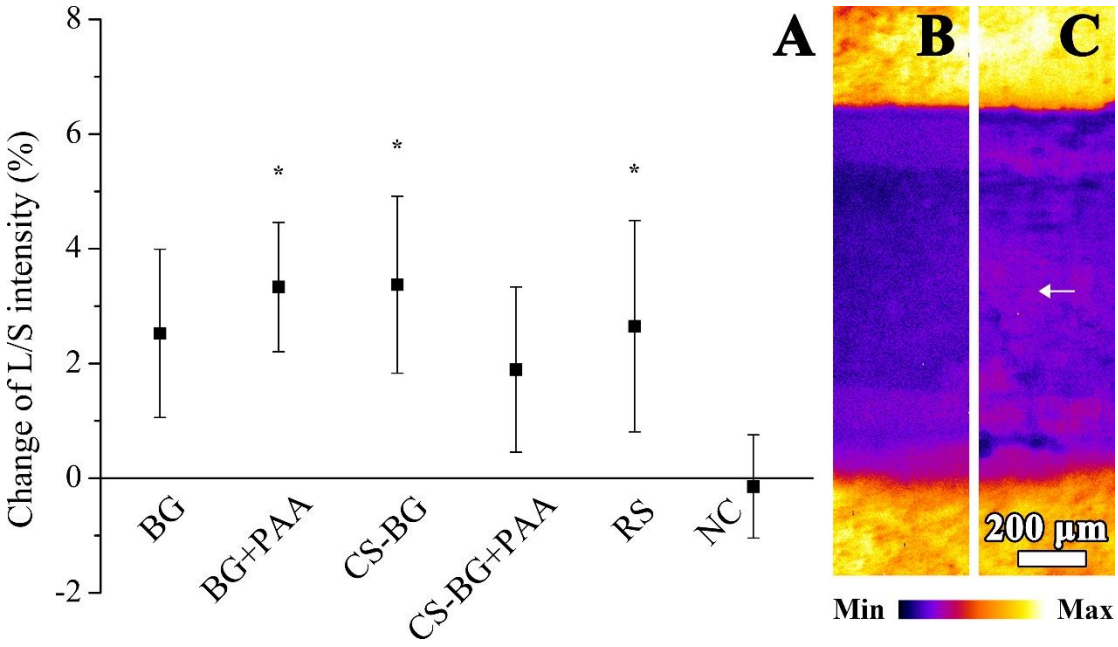

Fig. 3 Change of Raman intensity ratio after 7d remineralisation of all groups (a) and representative intensity maps of CS-BG+PAA before (b) and post (c) treatment. Increase of intensity ratio was found in all treatment groups, among which BG+PAA, CS-BG and RS groups showed significantly greater increase than NC. "*" indicates statistical difference comparing to NC ($p < 0.05$). With respect to the pseudocolour images, black denotes minimum intensity while white indicates maximum as indicated by the legend. After remineralisation, sample in CS-BG+PAA group showed increased intensity (white arrow) in the lesion area.

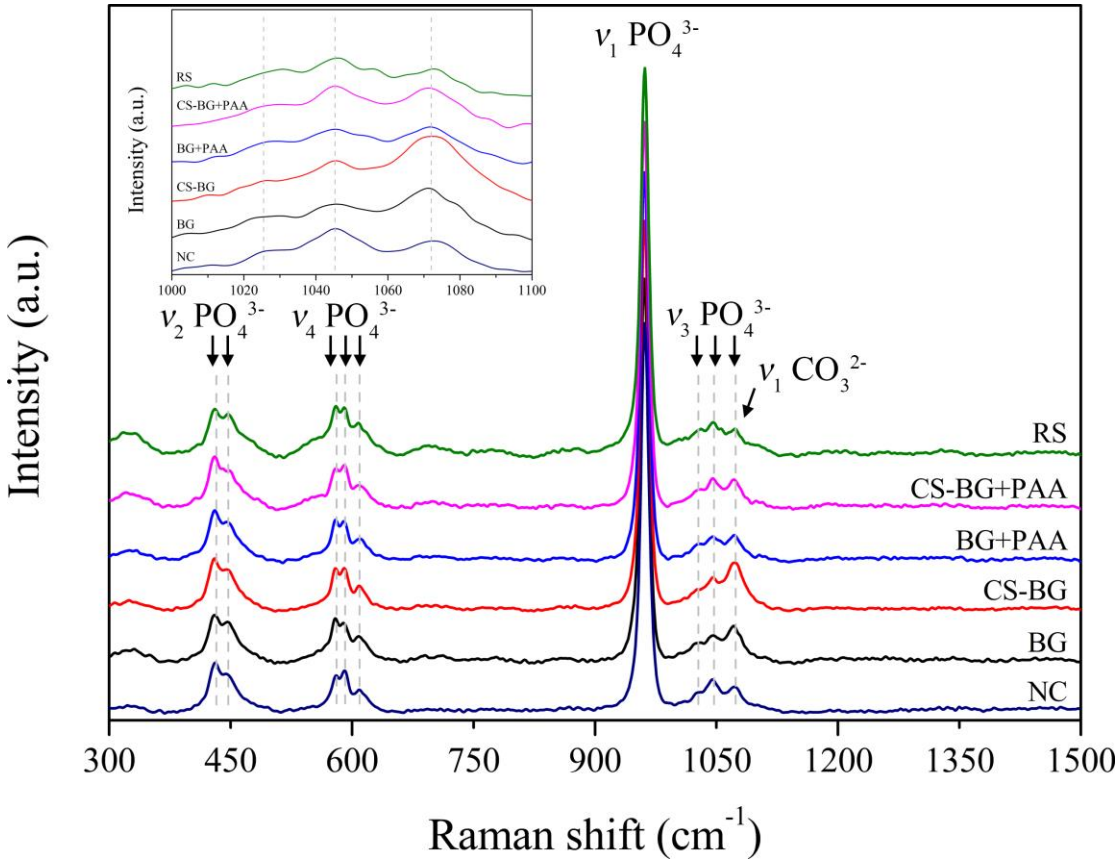

Fig. 4 Raman spectra of the lesion surfaces post remineralisation. Characteristic peaks of phosphate group appear at 961, 430, 446, 1030 and 1045 cm^{-1} in all groups, which are contributed by *v*1 asymmetric bending vibration, *v*2 symmetric bending vibration, *v*3 asymmetric stretching vibration and v*4* asymmetric stretching vibration of phosphate group, respectively (REF). The peak at 1071 cm^{-1} were attributed to both vibration of *v*3 PO_4^{3-} and *v*1 CO_3^{2-} and its relative intensity (compared to that at 1045 cm^{-1}) increased in all experimental groups except RS and NC, suggesting the formation of type-B HCA (REF). No significant change was found in terms of the intensity rations of 430 cm^{-1} to 446 cm^{-1} and 579 cm^{-1} to 589 cm^{-1} in all groups. Inset is the magnified spectra from 1000 to 1100 cm^{-1}.

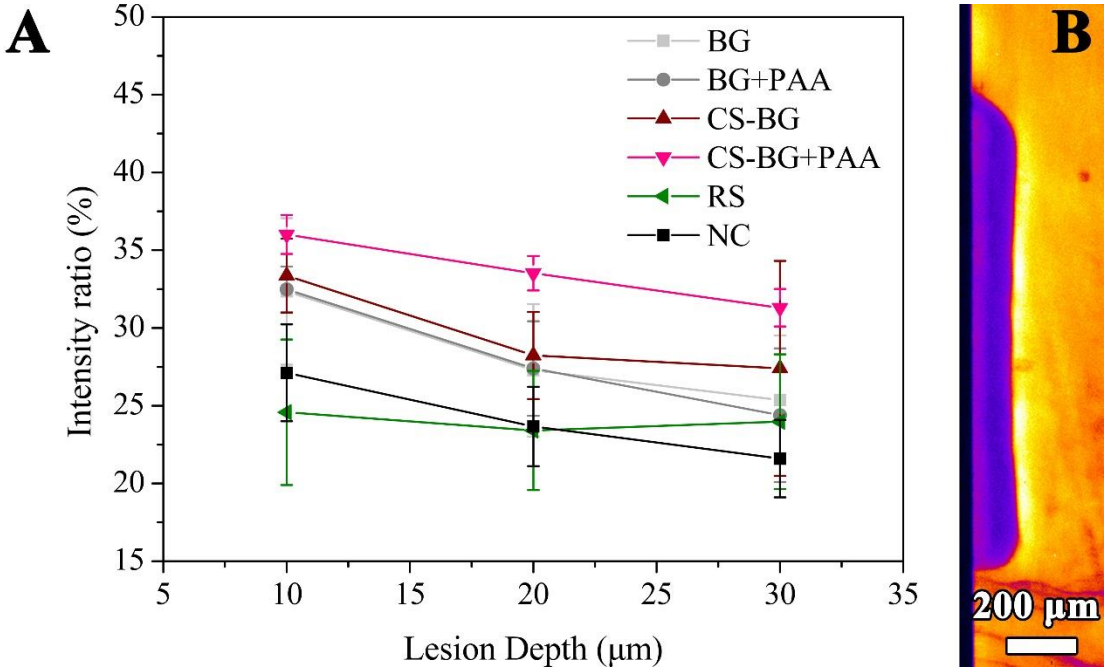

Fig. 5 Subsurface Raman intensity ratio (I_{lesion}/I_{sound}) at 10, 20 and 30 μm lesion depth below superficial surface post remineralisation (a) and representative intensity map of CS-BG+PAA (b). CS-BG+PAA showed the largest intensity ratio at all depth points and is significantly higher than NC ($p < 0.05$). BG, BG+PAA and CS-BG had similar intensity ratio at 10 and 20 μm. All groups also demonstrated similar trend, *i.e.* intensity ratio decreased with approaching deeper part of the lesion except RS at 30 μm. (b) presented a representative intensity map of the cross-section of CS-BG+PAA.

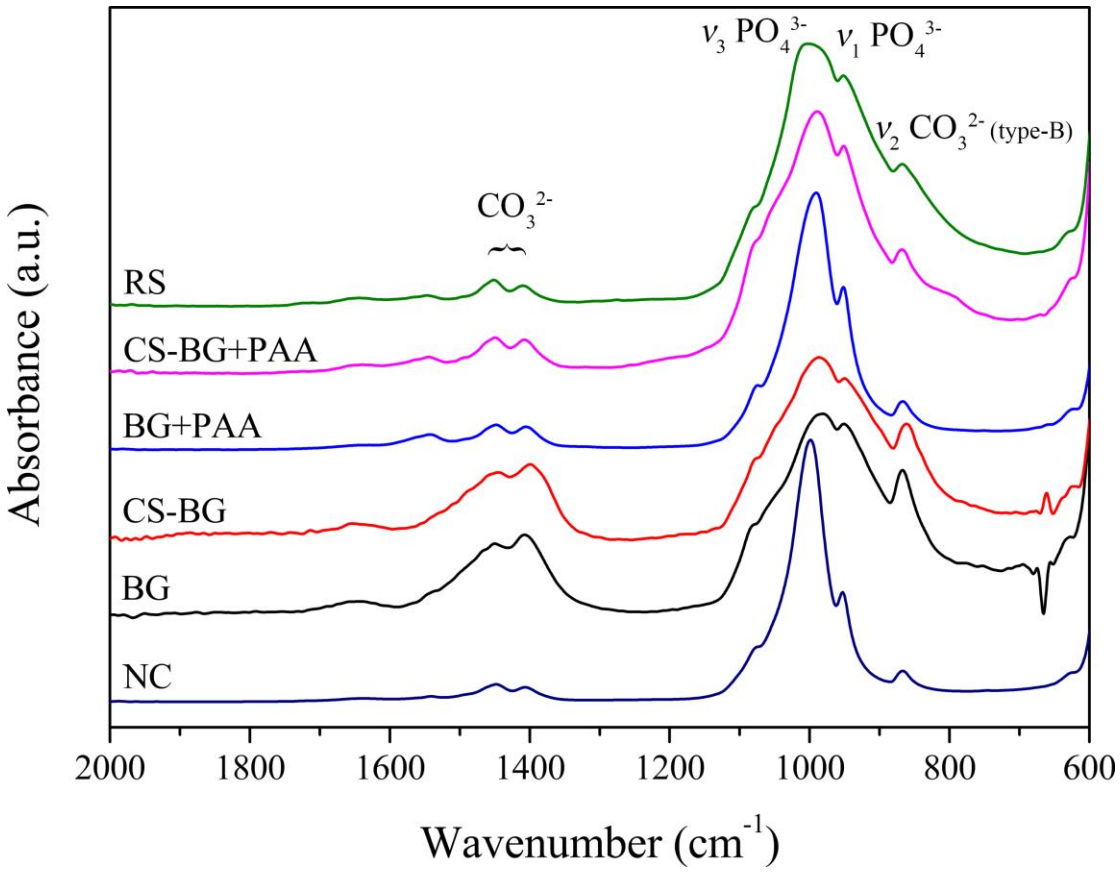

Fig. 6 ATR-FTIR spectra of the lesion surfaces post remineralisation. *v*3 PO_4^{3-} vibration contributed to the strongest band at 980 to 1000 cm^{-1}. A shoulder band appear at ~ 950 cm-1, attributed to *v*1 PO_4^{3-} vibration (REF). Redshift of *v*3 PO_4^{3-} vibration band to ~ 990 cm^{-1} was observed for all experimental groups except RS compared to that in NC (~ 1000 cm^{-1}). Two overlapping bands at 1400 to 1500 cm^{-1} can be seen in all groups, which are attributed to *v*3 CO_3^{2-} vibration (REF). Another carbonate band induced by *v*2 CO_3^{2-} vibration appear at ~ 867 cm^{-1}, while no obvious band appear at 880 cm^{-1}, indicating that no type-A HCA formed (REF). The intensities of these three bands increased post remineralisation in all experimental groups, suggesting the newly formed minerals included type-B HCA (REF).

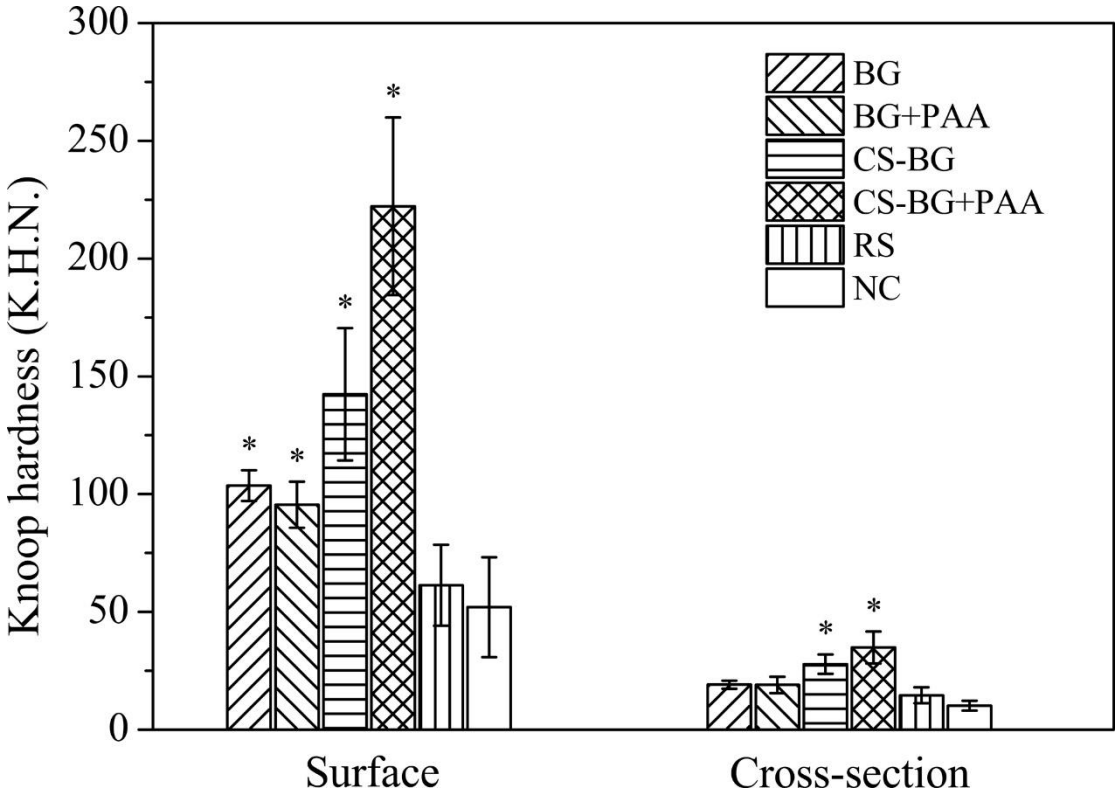

Fig. 7 Surface and cross-sectional microhardness of all samples after remineralisation. "*" indicates significant difference between CS-BG+PAA and other groups ($p < 0.05$). CS-BG+PAA had the greatest hardness recovery (222.2 ± 37.7), which is significantly higher than all other groups. Similarly, on cross-section (20 μm below superficial surface) CS-BG+PAA was the hardest among all groups ($p < 0.05$).

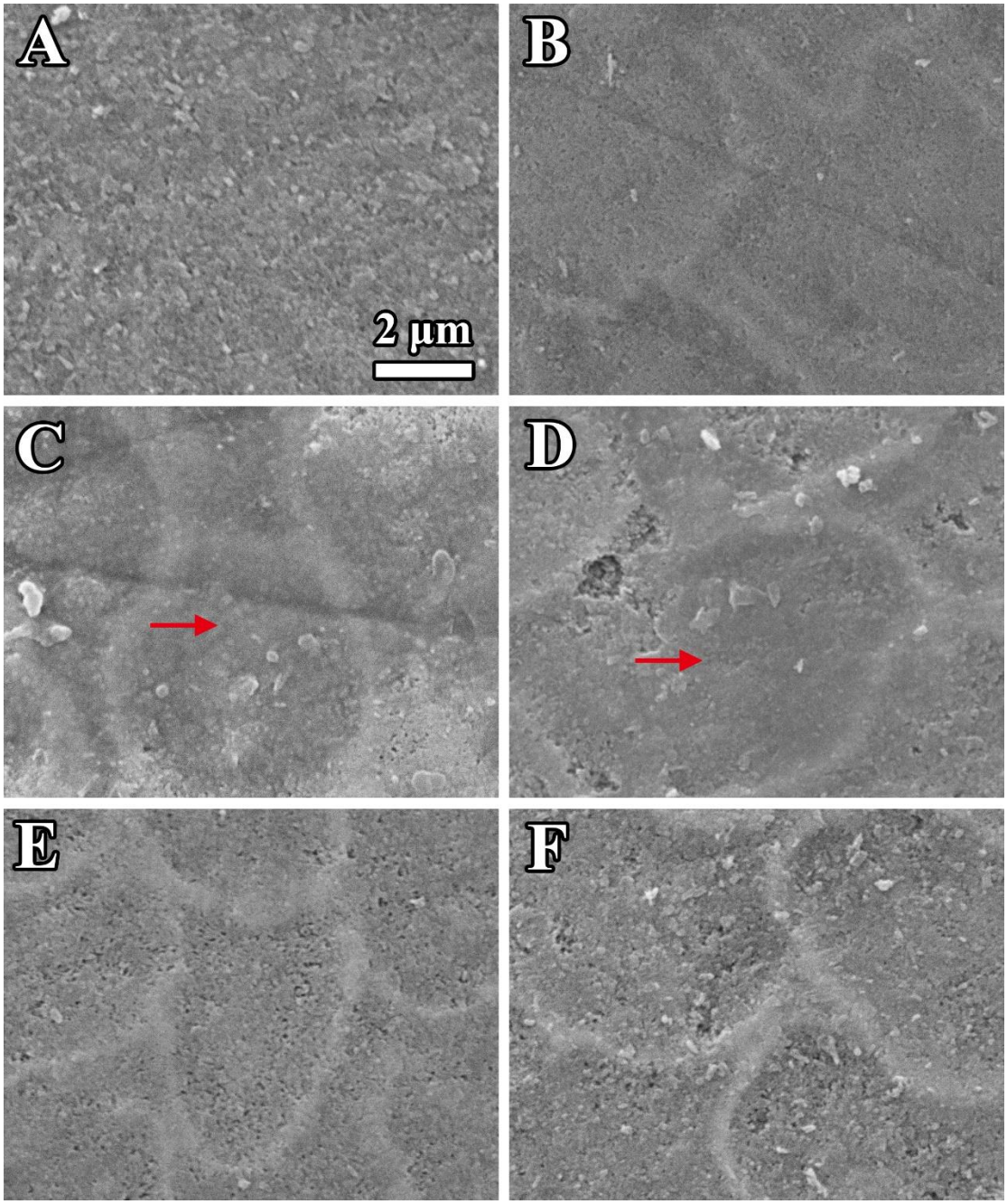

Fig. 8 Representative SEM images of surfaces after remineralisation. BG group (a) showed a dense packed precipitation layer. Prism structure could be seen in BG+PAA (b) with smaller pores. In CS-BG groups (c) and CS-BG+PAA (d), patch-like structures was clearly seen (red arrows) while some enlarged pores were also observed. With regards to RS (e) and NC (f), pores could be found within the prism. Small particles found in (f) could be due to the re-deposition of dissolved Ca/P ions caused by deionised water.

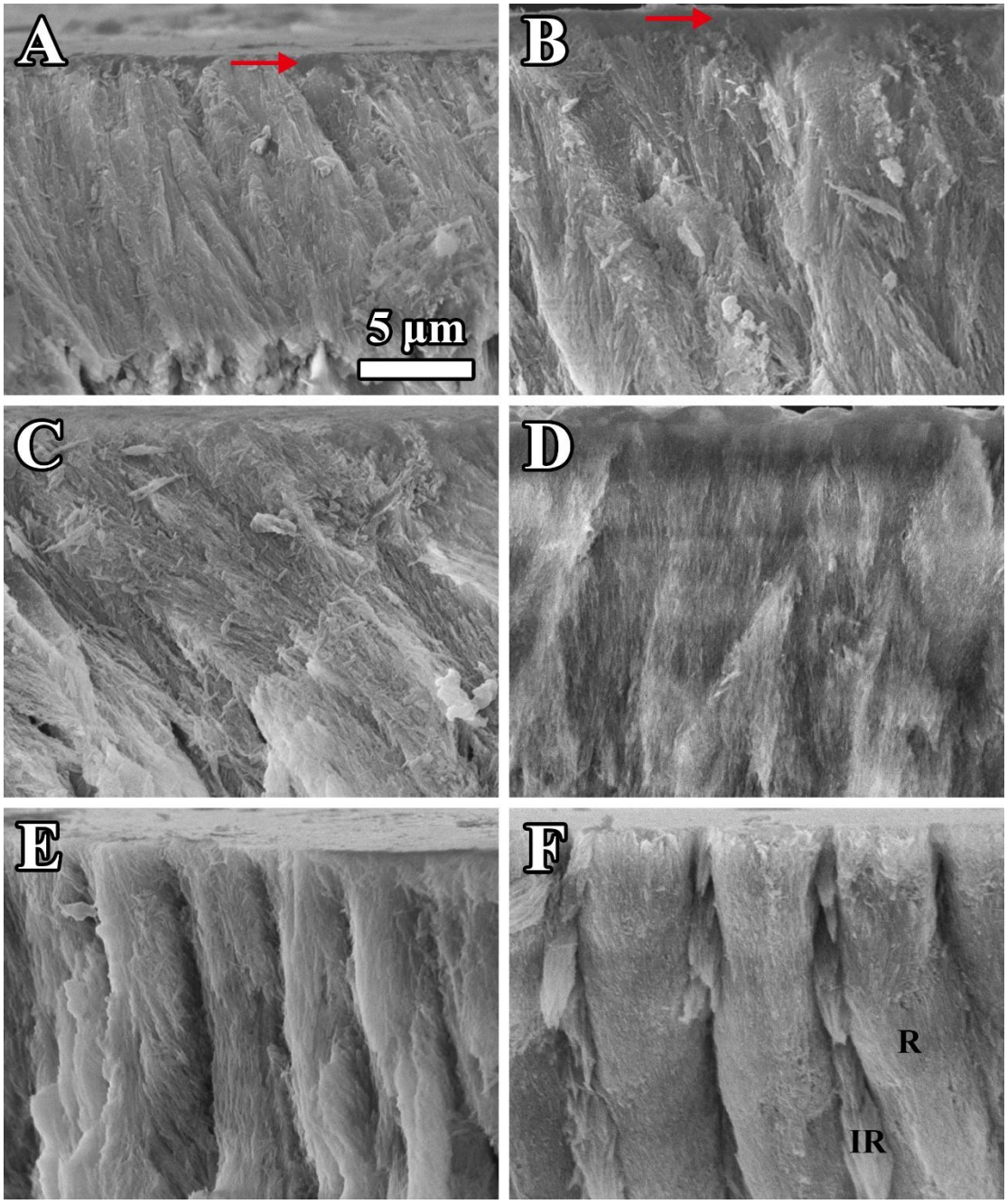

Fig. 9 Representative subsurface SEM images of fractured lesions of all groups after remineralisation. In BG (a) and BG+PAA (b), a newly precipitated layer were found to fill the gaps on the surface (red arrows). CS-BG (c) presented some subsurface non-oriented mineral depositions and disrupted prism structure, while CS-BG+PAA (d) showed a loss of prism structure. Prism (R) and gaps (IR) between prisms could be seen in both RS (e) and NC (f).

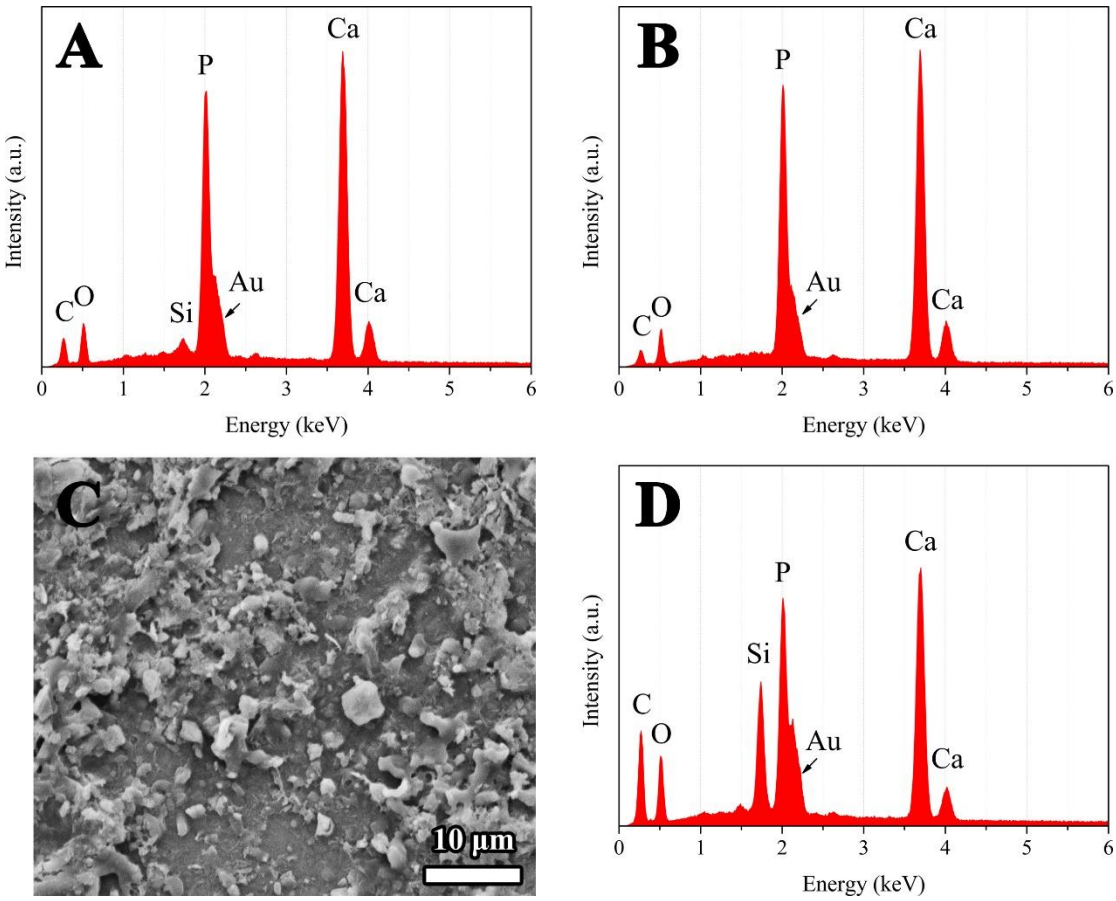

Fig. 10 Representative EDAX spectra of CS-BG+PAA (a), NC (b), SEM images of particles in CS-BG+PAA (c) and corresponding EDAX spectrum (d). Calcium, phosphorous, carbon, oxygen and gold were found to exist in all groups with similar distribution and peak height like in NC group (b), except that silicon was only present in CS-BG+PAA (a). Particles in CS-BG+PAA showed stronger silicon, carbon and oxygen peaks (d).